RSC Advances

PAPER

View Article Online
View Journal | View Issue

Cite this: *RSC Adv.*, 2018, **8**, 23268

Broadband near-infrared quantum cutting by Ce–Yb codoped YAG transparent glass ceramics for silicon solar cells

Yuping Tai, *[a] Xinzhong Li,*[b] Xigang Du,[a] Bingli Pan[a] and Guanghui Yuan[c]

Received 16th May 2018
Accepted 18th June 2018

DOI: 10.1039/c8ra04154g

rsc.li/rsc-advances

Ce^{3+}–Yb^{3+} co-doped transparent glass ceramics containing YAG nanocrystals were prepared by a conventional melt-quenching method. Broadband near infrared quantum cutting was achieved in the glass ceramics and proved to be a cooperative down-conversion process. Under 460 nm excitation, $^2F_{5/2}$ to $5d_1$ electronic transitions occurred in Ce^{3+} and transferred their energy to two neighboring Yb^{3+}. The dependence of the luminescence spectra and decay curves on Yb^{3+} concentration was investigated to understand the energy transfer mechanism. The energy transfer efficiency and the down-conversion quantum efficiency were estimated to be as high as 77.8% and 177.8%, respectively. This work will open a new route towards increased efficiency in silicon solar cells.

1. Introduction

Given the current energy crisis and increasing environmental pollution, it is imperative that new clean energy sources be developed. Since solar energy has many advantages, such as unlimited free energy without any undesirable environmental impacts, photovoltaics (PV) offer a unique opportunity to solve energy and environmental problems.[1,2] Among photovoltaic devices, silicon solar cells have attracted much attention due to their low cost and technological maturity. However, the conversion efficiency of silicon solar cells is only about 19%, which is much lower than the theoretical efficiency proposed by Shockley and Queisser.[3] The principal factor limiting the power conversion efficiency in silicon solar cells is the mismatch between the solar spectrum and the photoresponse spectrum. The bandgap of silicon is 1.12 eV and silicon solar cells can only absorb the NIR spectrum in the range of 900–1100 nm efficiently. As for UV-Vis wavelengths with high energy, energy is lost by thermalization. Unfortunately, the strongest portion of the solar spectrum lies in the 350–550 nm range, and this energy band (~2.3–3.5 eV) is twice the optical bandgap of silicon (~1.12 eV). Therefore, about 30% of incident solar radiation is lost due to thermalization.[4]

One effective way to reduce energy loss by thermalization is conversion of one high energy photon into two near-infrared (NIR) photons, which is known as quantum cutting (QC).[5] Lanthanide ions are ideal candidates for the QC process since the rich energy levels favor spectral absorption and QC.[6] Among rare earth (RE) ions, Yb^{3+} has simple energy levels that allow NIR emission at ~980 nm exclusively, which can be efficiently absorbed by silicon solar cells. Therefore, much attention has been focused on RE-Yb^{3+} (RE = Eu^{2+},[7,8] Pr^{3+},[9–11] Nd^{3+},[12–14] Er^{3+},[15–17] and Tb^{3+} (ref. 18–20)) co-doped powders, glasses, and glass ceramics (GC).

However, the majority of RE ions have low absorption cross-section that originates from parity forbidden 4f–4f transitions. This inhibits RE ions from absorbing broadband solar radiation and limits their energy transfer efficiency. In this case, Ce^{3+} is a good candidate because it allows 4f–5d transition and can absorb broadband solar radiation in the UV-Vis region. Moreover, the absorption spectrum of Ce^{3+} can be adjusted by changing the crystal field of the doped substrate. Therefore, a Ce^{3+}–Yb^{3+} co-doped system has attracted much attention in recent years.[21–25] Wang *et al.*[22] firstly reported Ce^{3+}–Yb^{3+} coupled QC in borate glasses, which can convert one absorbed UV photon at 330 nm into two NIR photons at 976 nm by the cooperative energy transfer (CET) process. However, the excitation spectrum of Ce^{3+} in borate glasses lies in the 200–400 nm region and cannot absorb the strongest solar radiation band. Borate glass also has disadvantages of poor chemical stability, mechanical stability, and high phonon energy, all of which limit the application of Ce^{3+}–Yb^{3+} co-doped borate glasses in silicon solar cell. Henceforth, a Ce^{3+}–Yb^{3+} co-doped system has been realized in YAG powder[23] and transparent ceramics.[24,25] The excitation spectrum of Ce^{3+} in YAG lies in the 300–500 nm region and matches the strongest solar radiation band. However, their applications have been limited due to the poor thermal stability.

[a]School of Chemical Engineering and Pharmaceutics, Henan University of Science and Technology, Luoyang, 471003, P. R. China. E-mail: yupingtai@126.com
[b]School of Physics and Engineering, Henan University of Science and Technology, Luoyang, 471003, P. R. China
[c]Department of Chemistry and Chemical Engineering, Ankang University, Ankang 725000, P. R. China

Transparent YAG GCs are excellent substrates for QC due to their low phonon energies, and high chemical and mechanical stability.[26,27] When RE ions are doped into YAG GCs, non-radiative relaxation can be suppressed efficiently and is beneficial to the CET process.

In this paper, transparent YAG GCs containing Ce^{3+}–Yb^{3+} pairs were synthesized by a traditional melt quenching method. It is remarkable that Ce^{3+} can efficiently absorb solar radiation in the 300–500 nm band, and subsequently convert one absorbed photon into two NIR photons *via* CET. The fluorescence lifetime was recorded to further verify the energy transfer (ET) mechanism and estimate the quantum efficiency (QE) of the down-conversion process between Ce^{3+} and Yb^{3+}. The result indicated that the maximal energy transfer efficiency (ETE) and down-conversion QE were 77.8% and 177.8% with 20.0 mol% Yb^{3+} concentration, respectively. The primary objective of the work is to increase the conversion efficiency in silicon solar cells with a twofold photon number increase.

2. Experimental

2.1 Oxyfluoride GC synthesis

The precursor glass was synthesized using a conventional quenching method with the following composition (in mol%): $60SiO_2$–$20Al_2O_3$–$10Yb_2O_3$–$10B_2O_3$–$0.5Sb_2O_3$: $1.0CeO_2$–xYb_2O_3 ($x = 0$, 1.0, 2.0, 5.0, 10.0, and 20.0). 20 g chemical batches with high purity (99.9%) were melted in a covered corundum crucible under a reducing atmosphere at 1500 °C for 0.5–1 h. Subsequently, the melt was cast into a preheated brass mold and annealed at 600 °C for 6 h to reduce the internal stress caused by thermal shock. To induce crystallization and obtain transparent YAG GCs, the as-prepared glass samples were heat treated (HT) for 8–12 h at different temperatures. The obtained glass samples under different HT temperatures were denoted HT740, HT760, HT780, and HT800, respectively.

2.2 Materials characterization

X-ray diffraction (XRD) analysis was performed on a D/Max-3C diffractometer with Cu Kα radiation (1.5405 Å, 40 kV, 60 mA) to identify the crystal phase and estimate the average crystallite size in the glass matrix. The microstructures of the glass samples were examined with a field emission scanning electron microscope (FE-SEM, Tescan, Mira/LMU) and a high-resolution transmission electron microscope (HRTEM, JEM-2010). Absorption spectra in the 400–1200 nm range were measured with a Perkin-Elmer UV/Vis/NIR Lambda 900 spectrophotometer. The excitation and emission spectra at both visible and NIR wavelengths were gathered with an FLS920 fluorescence spectrometer (Edinburgh Instruments, Britain). The fluorescence lifetime of the Ce^{3+} 531 nm emission line was recorded under 460 nm excitation with a tunable dye laser as the excitation source. All measurements were performed at room temperature.

3. Results and discussion

3.1 Structure behavior

The XRD patterns of the glass samples under different HT temperatures are presented in Fig. 1. One can clearly see that the HT740 sample shows a characteristic broad hump and reveals that the glass samples are amorphous. Upon increasing the temperature to 760 °C and maintaining for 12 h, sharp diffraction peaks appear in the XRD curve, which can be ascribed to separation of the orthorhombic YAG phase (JCPDS 30-0040) from the glass substrate. According to the Scherrer formula, the average YAG crystal size was determined to be about 15 nm in the HT760 sample. As the heat treatment temperature increased to 780 °C and 800 °C, the diffraction peaks become more intense due to the growth of YAG nanocrystals. The diameter of the YAG crystals increased to 100 nm in the HT780 sample, and they became much larger in the HT800 sample.

Fig. 2(a) shows a TEM image of the HT760 sample. One can clearly see that nanoparticles with ~10 nm diameter are homogenously distributed in the glass substrate, which are YAG crystalline grains according to the XRD results. The detailed structure of an individual YAG nanocrystal is shown in Fig. 2(b). The (HRTEM) image reveals the YAG nanoparticles have good crystallinity. The measured lattice spacing is 0.117 nm, which agrees with the (220) lattice plane of orthorhombic YAG and further verifies the XRD results.

3.2 Optical properties

The HT760 GCs was chosen as the doped substrate for the RE ions because of its homogeneous distribution and nano-sized diameter of the YAG crystalline grains. A batch of Ce^{3+}–Yb^{3+} co-doped GCs were prepared with 1.0 mol% Ce^{3+} concentration. The Yb^{3+} concentration was varied at 0, 1.0, 2.0, 5.0, 10.0, and 20.0 mol%. The Ce^{3+}–Yb^{3+} co-doped GCs with different Yb^{3+} concentrations are labeled YAG0, YAG1, YAG2, YAG3 YAG4, and

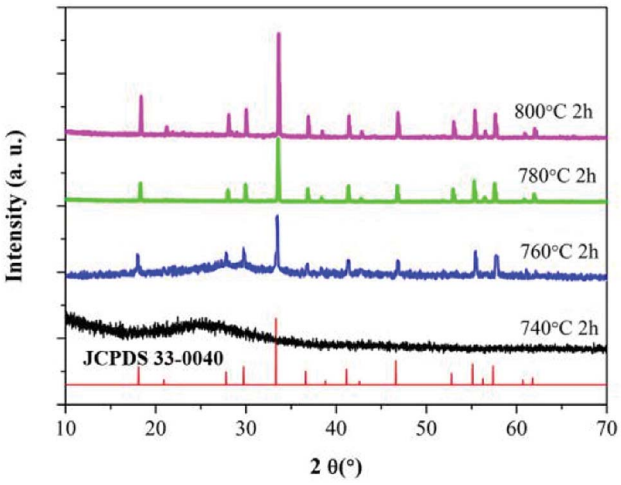

Fig. 1 XRD patterns of YAG glass: HT740, HT760, HT780 and HT800, respectively.

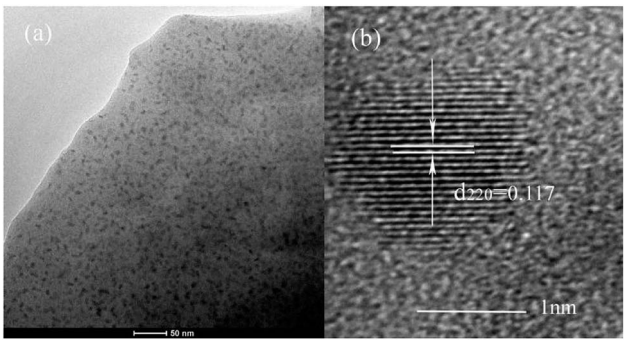

Fig. 2 (a) TEM micrograph of YAG GC under 760 °C heat-treatment (HT760) (b) HRTEM image of individual YAG nanocrystal.

YAG5, respectively. The absorption spectra for YAG0 to YAG5 are presented in Fig. 3. The results show that the absorption edge lies in the UV range and limits the glass transparency, and the absorption edge results from electronic transitions and oxygen impurities in the glass matrix.[12,13] Broadband absorption in the 400–500 nm range is ascribed to the Ce^{3+}: $^2F_{5/2} \rightarrow 5d_1$ transition. The other wide absorption band peaked at 980 nm is attributed to the Yb^{3+}: $^2F_{5/2} \rightarrow {}^2F_{7/2}$ transition. The absorption bands display identical positions and intensities in different GCs except for 980 nm peak, which becomes more intense with increasing Yb^{3+} concentration. From Fig. 3, one can conclude that the broadband radiation in the range of 400–500 nm and 900–1100 nm can be absorbed efficiently by Ce^{3+} and Yb^{3+}, respectively.

3.3 Down-conversion process from Ce^{3+} to Yb^{3+}

In order to investigate the ET process from Ce^{3+} to Yb^{3+} in the GC samples, excitation spectra of YAG1 and emission spectra from YAG0 to YAG5 were measured, and the results are shown in Fig. 4. One can see in Fig. 4(a) that the excitation spectrum consists of two broad peaks. The 300–400 nm band is assigned to the Ce^{3+}: $4f \rightarrow 5d_2$ transition, while the 400–500 nm band is assigned to the Ce^{3+}: $4f \rightarrow 5d_1$ transition. By monitoring the shape of excitation spectra in Yb^{3+} (980 nm) and Ce^{3+} (531 nm),

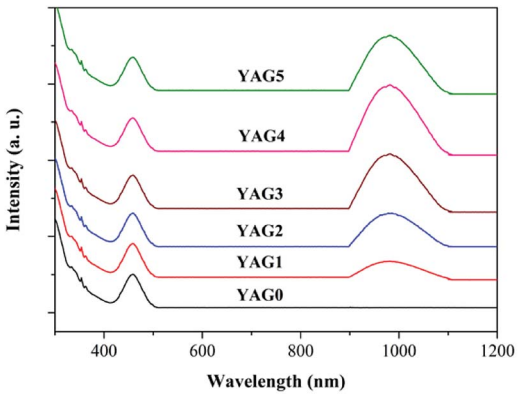

Fig. 3 Absorption spectra of Ce^{3+} single-doped (YAG0) and Ce^{3+}–Yb^{3+} co-doped samples (YAG1 to YAG5).

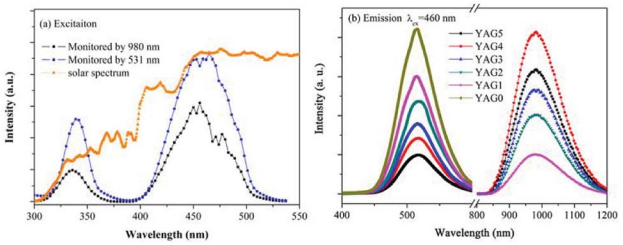

Fig. 4 (a) PLE spectra monitored by the Ce^{3+}: $5d_1 \rightarrow 4f$ transition (531 nm emission) and the Yb^{3+}: $^2F_{5/2} \rightarrow {}^2F_{7/2}$ transition (980 nm emission) in the YAG GCs. (b) PL spectra of Ce^{3+} and Yb^{3+} in the YAG GCs with different Yb^{3+} concentrations upon 460 nm excitation.

one can see that the emission lines are similar in YAG1. Because the solar radiation is strongest in the 350–550 nm range, the emission spectra from Ce^{3+} and Yb^{3+} were both recorded under 460 nm excitation, as shown in Fig. 4(b). For the Ce^{3+} singly doped sample (YAG0), there is only a broad emission peak at 531 nm due to the Ce^{3+}: $5d_1 \rightarrow 4f$ transition. As the Yb^{3+} concentration increased, the emission intensity from Ce^{3+} decreased significantly and the NIR emission from Yb^{3+} became stronger. However, the NIR emission became weaker when the Yb^{3+} concentration increased to 20.0 mol%, which revealed that concentration quenching (CQ) occurred between Ce^{3+} and Yb^{3+}.

To further verify the QC process and estimate the QE due to down-conversion between Ce^{3+} and Yb^{3+}, the excitation spectrum of YAG1 was monitored while emission from Yb^{3+} was recorded at 980 nm. This was then compared with the absorption spectrum of YAG1 in the UV-Vis region in Fig. 5. One can see that the absorption peak at 330 nm cannot be observed due to absorption in the GCs. In the excitation spectrum, the spectral region corresponding to the $4f \rightarrow 5d_1$ transition (460 nm) was integrated and found to be about 1.24 ± 0.1, and the corresponding absorption spectrum after integrating was approximately 0.68 ± 0.1. Taking into account the influence factor in

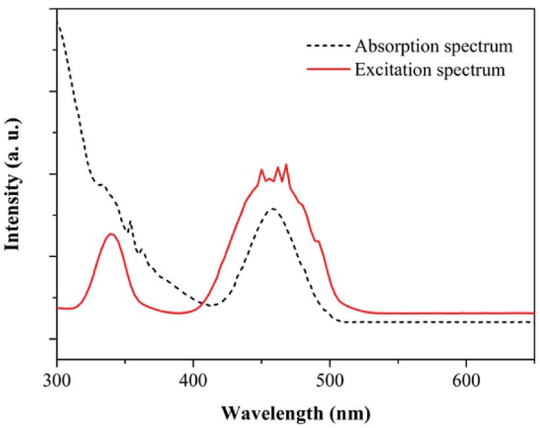

Fig. 5 Absorption and excitation spectra of the 1.0 mol% Ce^{3+}/1.0 mol% Yb^{3+} (YAG1) glass sample, demonstrating DC luminescence of Yb^{3+}. Excitation spectrum was recorded by monitoring Yb^{3+} emission at 980 nm and corrected for wavelength-dependent instrument response.

the experiment, the integrated excitation spectrum is nearly as twice that of the absorption spectrum, implying that ET from Ce^{3+} to Yb^{3+} is a QC process. Therefore, one incident photon in the 300–500 nm range can be converted into two NIR photons with a QE of approximately 180%. It is important to state that the actual QE value was much lower due to the 531 nm emission from Ce^{3+} and CQ of Yb^{3+}.

In order to explain the down-conversion mechanism in detail, the energy-level diagrams for Ce^{3+} and Yb^{3+} are shown in Fig. 6. The energy gap of the Ce^{3+}: $5d_1 \rightarrow 4f$ transition is nearly as twice that of the Yb^{3+}: $^2F_{7/2} \rightarrow {}^2F_{5/2}$ transition, which enables possible cooperative down-conversion from Ce^{3+} to Yb^{3+}. As a result, the Ce^{3+} decay rate is accelerated and the emission intensity of Yb^{3+} is enhanced by the cooperative down-conversion process. The down-conversion mechanism can be depicted as Ce^{3+}: $5d_1 \rightarrow Yb^{3+}$: $^2F_{5/2} + Yb^{3+}$: $^2F_{5/2}$, which agrees with the reports of Lin *et al.* According to the down-conversion process, a single green photon absorbed by Ce^{3+} ions is converted into two ~980 nm photons, which are then absorbed by the solar cell.

3.4 Decay curves and energy transfer efficiency

The decay curves for Ce^{3+}: $4f \rightarrow 5d_1$ emission at 531 nm were recorded for different Yb^{3+} concentrations, and the results are shown in Fig. 7. The experimental lifetime (τ_m) in different YAG GCs can be estimated using eqn (1)

$$\tau_m = \int I(t)dt / I_p, \quad (1)$$

where $I(t)$ is the luminescence intensity at some time t after the excitation light has been cut off, and I_p is the peak intensity in the decay curve. 531 nm emission from YAG0 indicates nearly single exponential decay. With increasing Yb^{3+} concentration, the decay curves gradually deviate from single exponential decay. Meanwhile, the obtained lifetime shows a rapid decrease with increasing Yb^{3+} concentration. The lifetime of YAG0 is estimated 6.13 μs, and it decreases to 5.8, 4.73, 3.82, 2.08 and 1.38 μs with increasing the Yb^{3+} concentration from YAG1 to YAG5. Since the Ce^{3+} concentration is fixed to 1.0 mol% in the different GCs, the observed changes in the decay curves and the decreasing lifetime could be explained by the introduction of an extra decay route (CET from Ce^{3+} to Yb^{3+}).

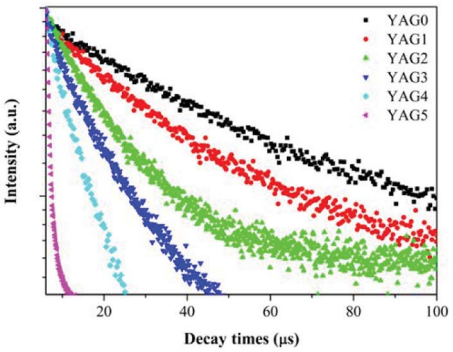

Fig. 7 Room temperature lifetime measurements of Ce^{3+}: $5d_1 \rightarrow 4f$ transition (531 nm emission) upon 460 nm excitation.

The energy transfer in the Yb^{3+} : Ce^{3+} system is a resonant process, which can be discussed according to the Forster–Dexter theory of non-radiative energy transfer between the impurities (sensitizer and activator) in solids.[28] Such a model is based on the electrostatic interactions between the impurities and can occur by means of dipole–dipole, dipole–quadrupole, or quadrupole–quadrupole coupling. Some studies have shown that dipole–dipole interaction is the dominant mechanism for energy transfer.[29–31] And the macroscopic energy transfer rate by dipole–dipole interaction can be evaluated by the following equation:[31]

$$P_{s-a} = \frac{1}{\tau} - \frac{1}{\tau_0} \quad (2)$$

where, τ_0 and t represent the decay time of the sensitizer emission in the singly and co-doped samples, respectively.

Using eqn (2), the energy transfer rate of different samples are calculated.

According to Dexter,[32] if one neglects the non-radiative transitions in the sensitizers, the energy transfer efficiency (ETE) can be evaluated by the equation,[33]

$$\eta_{ETE} = \frac{P_{s-a}\tau_0}{1 + P_{s-a}\tau_0} \quad (3)$$

where P_{s-a} is the sensitizer-activator energy transfer probability. The values of P_{s-a} and η_{s-a} for all the YAG GCs are

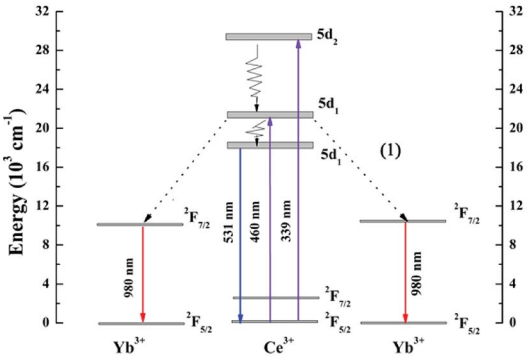

Fig. 6 Schematic energy level diagram of Ce^{3+}, Yb^{3+} ions, showing the CET process from Ce^{3+} to Yb^{3+} under 460 nm excitation.

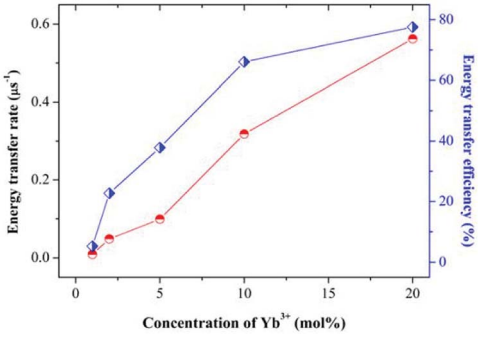

Fig. 8 The energy transfer rate (P_{s-a}) and energy transfer efficiency (ETE) between the Ce^{3+} and Yb^{3+} as a function of Yb^{3+} concentrations from YAG0 to YAG5.

plotted as a function of Yb^{3+} concentration and shown in Fig. 8. It is notable that the high energy-transfer rates are obtained in YAG GCs, and it increases rapidly from 0.009 to 0.562 μs^{-1} when Yb^{3+} concentration increases to 20 mol%. Correspondingly, for the best emitting sample at 980 nm (1 mol% Ce^{3+} : 20 mol%Yb^{3+}), it can be evaluated that the η_{s-a} is 77.6% approximately with $P_{s-a} = 0.562\ \mu s^{-1}$ and $\tau_0 = 6.13\ \mu s$. All of the results further confirm that the energy transfer occurs from Ce^{3+} to Yb^{3+} and is accelerated with Yb^{3+} concentration increasing."

The theoretical down-conversion quantum efficiency (QE), defined as the ratio of the number of emitted photons to the number of absorbed photons, can be estimated using the following equation[12]

$$QE = \eta_{Ce}(1 - \eta_{ETE}) + 2\eta_{ETE} \quad (4)$$

where η_{Ce} is the QE of Ce^{3+}, which is assumed to be 1 according to previous reports.

Under the assumption of $\eta_{Ce} = 1$, it can be calculated that the QE for YAG1 to YAG5 are 105.2%, 122.7%, 137.8%, 166.2%, and 177.8%, respectively. It is important to note that the actual QE was lower than theoretical value because of the 531 nm emission from Ce^{3+}.

4. Conclusions

In summary, Ce^{3+}–Yb^{3+} co-doped GCs containing YAG nanocrystals were prepared by a conventional melt-quenching method. Broadband NIR QC was achieved *via* a CET process from Ce^{3+} to Yb^{3+}, which was verified experimentally by analyzing the luminescence properties. The optimal theoretical ETE and QE were estimated to be 77.8% and 177.8%, respectively. According to the down-conversion process, one incident photon absorbed by Ce^{3+} can be converted into two NIR photons at 980 nm by Yb^{3+}, and then are efficiently utilized by silicon-based solar cells. Therefore, the Ce^{3+}–Yb^{3+} co-doped transparent YAG GCs might be useful as a down-conversion layer to increase the conversion efficiency of silicon solar cells, which can take full advantage of solar radiation in the 350–550 nm range.

Conflicts of interest

There are no conflicts to declare.

Acknowledgements

This work was supported by the National Natural Science Foundation of China (No. 51675162, 61775052, 61205086), Education Department Project of Henan Province (No. 18B150005), Open Research Fund of State Key Laboratory of Transient Optics and Photonics, Chinese Academy of Sciences (SKLST201203), Foundation for University Key Teacher of Henan Province (No. 2013071), Natural Science Fund of Education Department of Shaanxi Provincial Government (Grant No. 16JK1018), Natural Science Fund and Subject Merging Fund of Ankang University for high-level talents (Grant No. 2016AYQDZR05 and 2017AYJC01), and Key Project of Industrial Science and Technology of Shaanxi Province (No. 2016GY-196).

Notes and references

1 N. N. Zhang, Y. Zhang and J. Bao, *Chin. Opt. Lett.*, 2017, **15**, 063501.
2 S. Gu, P. C. Zhu and R. X. Lin, *Chin. Opt. Lett.*, 2017, **15**, 093501.
3 W. Shockley and H. J. Queisser, *J. Appl. Phys.*, 1961, **32**, 510–519.
4 B. S. Richards, *Sol. Energy Mater. Sol. Cells*, 2006, **90**, 1189–1207.
5 T. Trupke, M. A. Green and P. Wurfel, *J. Appl. Phys.*, 2002, **92**, 1668–1674.
6 B. M. van der Ende, L. Aarts and A. Meijerink, *Phys. Chem. Chem. Phys.*, 2009, **11**, 11081–11095.
7 H. Lin, D. Q. Chen and Y. L. Yu, *J. Alloys Compd.*, 2011, **509**, 3363–3366.
8 J. J. Zhou, Y. X. Zhuang and S. Ye, *Appl. Phys. Lett.*, 2009, **95**, 141101.
9 B. M. van der Ende, L. Aarts and A. Meijerink, *Adv. Mater.*, 2009, **21**, 3073–3077.
10 A. Jaffrès, B. Viana and E. van der Kolk, *Chem. Phys. Lett.*, 2012, **527**, 42–46.
11 C. G. Ming, F. Song and L. Q. An, *Curr. Appl. Phys.*, 2014, **14**, 1028–1030.
12 D. Q. Chen, Y. L. Yu and H. Lin, *Opt. Lett.*, 2010, **35**, 220–222.
13 J.-M. Meijer, L. Aarts and B. M. van der Ende, *Phys. Rev. B: Condens. Matter Mater. Phys.*, 2010, **81**, 035107.
14 Y. P. Tai, X. Z. Li and B. L. Pan, *J. Lumin.*, 2018, **195**, 102–108.
15 J. J. Eilers, D. Biner and J. T. van Wijngaarden, *Appl. Phys. Lett.*, 2010, **96**, 151106.
16 L. Aarts, B. M. van der Ende and A. Meijerink, *J. Appl. Phys.*, 2009, **106**, 023522.
17 S. R. Lüthi, H. U. Güdel and M. P. Hehlen, *J. Chem. Phys.*, 1999, **110**, 12033–12043.
18 Q. Y. Zhang, G. F. Yang and Z. H. Jiang, *Appl. Phys. Lett.*, 2007, **91**, 051903.
19 S. Ye, B. Zhu and J. Chen, *Appl. Phys. Lett.*, 2008, **92**, 141112.
20 X. Liu, S. Ye and Y. Qiao, *Appl. Phys. B*, 2009, **96**, 51–55.
21 J. D. Chen, H. Guo and Z. Q. Li, *Opt. Mater.*, 2010, **32**, 998–1001.
22 D. Q. Chen, Y. S. Wang and Y. L. Yu, *J. Appl. Phys.*, 2008, **104**, 116105.
23 X. Liu, Y. Teng and Y. Zhuang, *Opt. Lett.*, 2009, **34**, 3565–3567.
24 J. Ueda and S. Tanabe, *J. Appl. Phys.*, 2009, **106**, 043101–043105.
25 H. Lin, S. M. Zhou and H. Teng, *J. Appl. Phys.*, 2010, **107**, 043107.
26 J. Li, J. Liu and B. Liu, *J. Eur. Ceram. Soc.*, 2014, **34**, 2497–2507.
27 L. Wang, L. Mei and G. He, *J. Lumin.*, 2013, **136**, 378–382.
28 D. L. Dexter, *J. Chem. Phys.*, 1953, **21**, 836–850.

29 M. A. Chamarro and R. Cases, *J. Non-Cryst. Solids*, 1989, **107**, 178–186.
30 S. Tanabe, T. Kouda and T. Hanada, *Opt. Mater.*, 1999, **12**, 35–40.
31 Z. G. Nie, J. H. Zhang and X. Zhang, *J. Solid State Chem.*, 2007, **180**, 2933–2941.
32 R. Reisfeld and N. Lieblich-sofer, *J. Solid State Chem.*, 1979, **28**, 391–395.
33 D. L. Dexter, *J. Chem. Phys.*, 1953, **21**, 836–850.